



## Detailed study of the distribution of activation inside the magnet coils of a compact PET cyclotron

V. Bonvin<sup>a,b,\*</sup>, F. Bochud<sup>b</sup>, J. Damet<sup>b,d</sup>, C. Theis<sup>a</sup>, H. Vincke<sup>a,c</sup>, R. Geyer<sup>a,b</sup>

<sup>a</sup> European Council for Nuclear Research (CERN), Esplanade des Particules, CH-1211, Meyrin, Switzerland

<sup>b</sup> Institute for Radiation Physics, Lausanne University Hospital, Rue du Grand-Pré, CH-1007, Lausanne, Switzerland

<sup>c</sup> University of Technology, Rechbauerstraße 12, 8010, Graz, Austria

<sup>d</sup> University of Otago, 2 Riccarton Ave, Christchurch, New Zealand

### ARTICLE INFO

#### Keywords:

Cyclotron  
Gamma spectrometry  
Monte Carlo simulation  
Positron emission tomography  
Neutron spectrum  
Magnet coil  
Activation  
Decommissioning

### ABSTRACT

We determined the distribution of activation products inside the magnet coils of a medical cyclotron that has been operational for fifteen years. Besides FLUKA, we based our approach on new software tools (RAW and ActiWiz) developed for high-energy accelerators at CERN. A combined analysis of measurements on the coils with Monte-Carlo simulations resulted in a detailed three-dimensional radiological characterisation of the coils. Our results provide the required information for the radiation protection expert to identify the appropriate waste elimination scheme.

### 1. Introduction

Recently published data from the statistical office of the European Union (Eurostat, 2019a) shows a clear trend of increasing Positron Emission Tomography (PET) examinations in Europe for the 2012–2017 period. This trend is also confirmed by the fact that the number of PET scanners in France has almost doubled within the same period (Eurostat, 2019b). The fast development of nuclear medicine over the last few decades has involved the construction of production centres for short-lived radioisotopes using medical cyclotrons. More than 1200 of such centres have been registered worldwide by the IAEA (IAEA, 2019). Half of these cyclotrons are operating with energies between 16 and 19 MeV. The radioisotopes, which are typically used for PET examinations, are <sup>18</sup>F, <sup>11</sup>C and <sup>13</sup>N (IAEA, 2009), with half-lives of 109.7 min, 20.38 min and 9.97 min, respectively.

Alongside the obvious medical benefits, the use of particle accelerators also raises radiation protection issues. The components of the accelerator and its environment (bunker) may become radiologically activated during the operation phase. When cyclotron facilities are decommissioned, all their components must be radiologically characterised. The components shall be treated according to the local regulations (IAEA, 2003). The radiological characterisation represents the

determination of the nature, location and concentration of radionuclides at a nuclear installation (NEA, 2013). This definition is also valid for accelerator facilities, where the radioactivity is artificially induced. A good understanding of the activation processes taking place inside and near the cyclotron is essential for an efficient characterisation. This is essential in order to establish the appropriate decommissioning procedure.

For this study, we conducted a detailed examination of a type IBA-Cyclone 18/9 cyclotron. After fifteen years of operation, the magnet coils were replaced during a technical service. The operation of the machine was continued after repair. The radiological characterisation of these coils became necessary in order to identify the most appropriate disposal path. In this case, the characterisation is equivalent to the determination of the three-dimensional distribution of activities of the activation products, which are relevant to determine the hazardousness of the material. To obtain the distributions, we combined results of  $\gamma$ -ray measurements of material samples of the coils with the results from Monte-Carlo simulations.

Several studies have already been published about the activation products inside materials of different medical cyclotrons (Calandrino et al., 2006) (Sunderland et al., 2012). They have estimated the total activities of the most important radionuclides produced inside several

\* Corresponding author. European Council for Nuclear Research (CERN), Esplanade des Particules, CH-1211, Meyrin, Switzerland.

E-mail address: [valentin.bonvin@cern.ch](mailto:valentin.bonvin@cern.ch) (V. Bonvin).

<https://doi.org/10.1016/j.apradiso.2020.109446>

Received 4 June 2020; Received in revised form 22 September 2020; Accepted 24 September 2020

Available online 28 September 2020

0969-8043/© 2021 The Authors. Published by Elsevier Ltd. This is an open access article under the CC BY license (<http://creativecommons.org/licenses/by/4.0/>).

components at these facilities. However, details about the distribution of the specific activities within these materials were not presented, which could deliver additional information for the characterisation and an optimised decommissioning procedure.

A recent article (Toyoda et al., 2018) about the induced activity in various components of PET-cyclotrons has examined the radionuclides that were induced in the metal components. The cyclotrons were of type IBA-Cyclone 10/5 and JSW-BC1710. They determined the depth distribution of the activation by extracting core samples on several components. Gamma-spectroscopy results are available for several locations of the yokes and the sector magnets. Only dose rate measurements are presented for the samples of the magnet coils. Detailed information on the distribution of activation inside the magnet coils is not given.

Here we give, for the first time, a complete and seamless picture regarding the distribution of the activation products over the full volume of the magnet coils of a medical cyclotron.

Because of its low energy (18 MeV), the proton beam is stopped after a few millimetres in matter (e.g. 3.5 mm in water). The target assemblies for the production of isotopes are integrated into the vacuum chamber. This means that beam protons cannot contribute directly to the activation of the magnet coils or any other element outside of the vacuum chamber. The activation of the coils is induced by secondary neutrons, which originate from interactions of the beam particles with the different target assemblies or with materials inside the vacuum chamber of the cyclotron. A good understanding of these neutron fields is essential for the successful characterisation of materials in and around the cyclotron. For this work, we implemented a consistent description of all relevant sources of secondary neutrons into a Monte-Carlo model for the cyclotron using FLUKA. Following FLUKA, ActiWiz and RAW were then applied in order to reduce the required computing time and to automate the analysis. The latter two are software tools developed at CERN for the characterisation of activated material at accelerators. This is the first time they are being applied for medical cyclotrons. We then compared the simulation results with those from  $\gamma$ -ray spectrometry. The following sections summarise the radiological characterisation of

the coils. The methodology described here can also be applied to other components of cyclotron facilities in order to obtain detailed information about the distribution of activations.

## 2. Materials and methods

### 2.1. Description of the biomedical cyclotron IBA cyclone 18/9

We studied a Cyclone 18/9 cyclotron from IBA that has been in operation since 2000 for the routine production of radioisotopes in a hospital unit. It is a compact accelerator with an energy of 18 MeV and a nominal beam intensity of 150  $\mu$ A, which corresponds to  $9.36 \times 10^{14}$  protons/s. Furthermore, the accelerator can be operated with both protons and deuterons. However, for this study, the second option was used for the production of  $^{15}\text{O}$  for two days only. The cyclotron has eight target ports used for the production of radioisotopes. Fig. 1 shows the most important components of the cyclotron: the deep valley magnet with yoke, poles and coils, the dual ion source, the dees for the acceleration of particles, the vacuum chamber and the targets. The cyclotron is mainly used for the production of  $^{18}\text{F}$ ,  $^{13}\text{N}$ , and  $^{11}\text{C}$  by using different target materials (liquid or gas). The key parameters of the machine and

**Table 1**  
Main characteristics of the Cyclone 18/9 Cyclotron (IBA, 2009).

Energy (MeV)	proton	18
	deuteron	9
Intensity ( $\mu$ A)	proton	150 ( $9.36 \times 10^{14}$ p/s)
	deuteron	40 ( $2.50 \times 10^{14}$ d/s)
Particles sources	2 separate Penning Ion Gauge ion sources	
Number of target ports	8	
Simultaneous target beams	2	
Mean field (T)	1.35	
Weight (kg)	25,000	

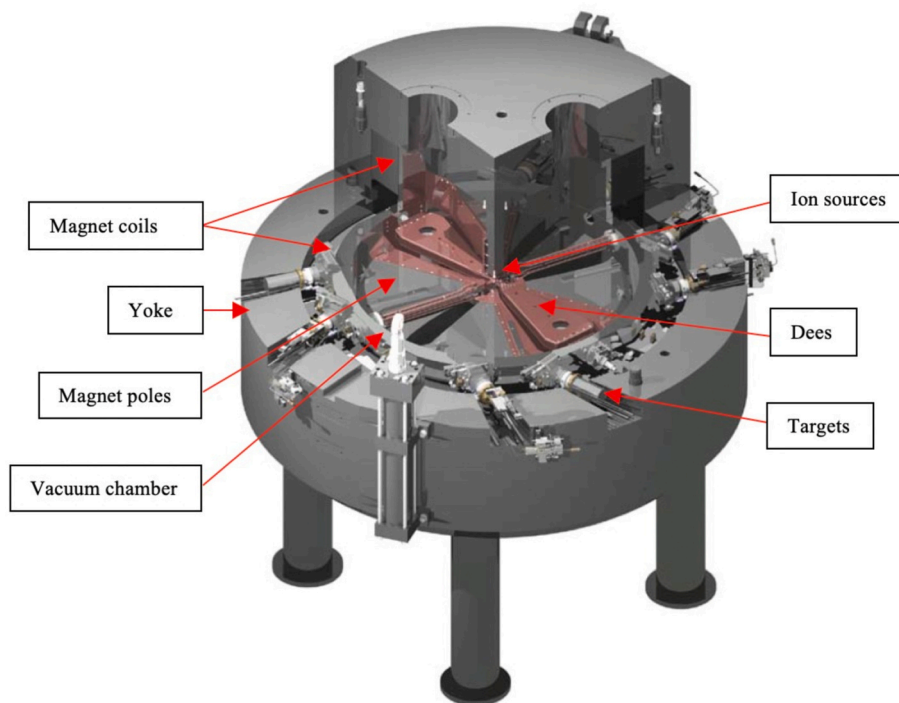


**Fig. 1.** Sketch of the Cyclone 18/9 cyclotron (IBA, 2009). (For interpretation of the references to color in this figure legend, the reader is referred to the Web version of this article.)

the characteristics of the different targets are summarized in Table 1 and Table 2, respectively. The main characteristics of the coils are given in Table 3. The copper of the coils follows the standard OFCu (oxygen free copper) type C1020 with a high purity better than 99.96%. Further details about this cyclotron can be found in the documents provided by the company (IBA, 2009).

The machine operators provided us with the required information about the operation of the cyclotron. In the years between 2005 and the end of 2015, the date when the coils were replaced, the cyclotron was mainly used for the production of  $^{18}\text{F}$  and  $^{13}\text{N}$  with the occasional production of small batches of  $^{11}\text{C}$ . A typical example: a total activity of 26 TBq of  $^{18}\text{F}$  and 1 TBq of  $^{13}\text{N}$  were produced in 2017. Unfortunately, we did not receive any data for operations conducted before 2005.

## 2.2. Estimation of the activation of the magnet coils by simulation

The activation of the coils is caused by the secondary neutrons produced by the interactions of the beam protons with components of the accelerator within the vacuum chamber. Two mechanisms for the production of secondary neutrons can be distinguished.

The first mechanism corresponds to the interactions of the nominal beam with materials on its trajectory, *i.e.* the stripper foils composed of few microns of carbon (Braccini, 2016) and the target ports. Each target port includes the collimator, the vacuum window, the target window and the target material, which is used to produce the radioisotopes of interest.

The second mechanism corresponds to “unwanted” beam losses. One reason for this is due to the dissociation of  $\text{H}^-$  ions by the residual gas inside the vacuum chamber (Papash and Alenitsky, 2008). The resulting H atoms are no longer guided by the magnetic field. They will continue tangentially from the point of ionization until they hit a material - most likely the vacuum chamber. The losses are in the order of 50% of the accelerated beam (Papash and Alenitsky, 2008). Other beam losses except from ionization are not taken into account here.

Two analysis steps are needed to determine the three-dimensional distribution of activation produced inside the coils:

1. Estimation of the fluence of the secondary neutrons inside the coils with the help of the Monte Carlo tool FLUKA version 3.0 (Böhlen et al., 2014; Ferrari et al., 2005).

2. Estimation of the activation products and their activities with the help of the software tools ActiWiz version 1.3.168 (Vincke and Theis, 2018) and RAW version 4.1.2 (Geyer et al., 2019).

### 2.2.1. Estimation of the fluence of secondary neutrons

The present study seeks to evaluate the fluence of secondary neutrons inside the coils by implementing a simplified geometrical model of the cyclotron in FLUKA. FLUKA is a Monte Carlo simulation package for the interaction and transport of particles and nuclei in matter. It is widely used in the environment of accelerators.

As a first working hypothesis, we assumed that only interactions of the nominal beam particles with the eight target ports had to be taken

**Table 2**  
Characteristics of the different target types (IBA, 2009).

Isotope produced	Chemical form	Target reaction	Target material	Vacuum window	Target window
$^{11}\text{C}$	$\text{CO}_2$	$^{14}\text{N}$ ( $\text{p},\alpha$ ) $^{11}\text{C}$	$\text{N}_2+$ 0.5–1% $\text{O}_2$	12 $\mu\text{m}$ Titanium	500 $\mu\text{m}$ Aluminium
$^{13}\text{N}$	$\text{NH}_3$	$^{16}\text{O}$ ( $\text{p},\alpha$ ) $^{13}\text{N}$	$\text{H}_2\text{O}$ (natural) +5 mMol Ethanol	12 $\mu\text{m}$ Titanium	25 $\mu\text{m}$ Havar®
$^{15}\text{O}$	$\text{O}_2$	$^{14}\text{N}(\text{d},\text{n})^{15}\text{O}$	$\text{N}_2+ 0.5\%$ $\text{O}_2$	12 $\mu\text{m}$ Titanium	50 $\mu\text{m}$ Havar®
$^{18}\text{F}$	$\text{F}^-$	$^{18}\text{O}(\text{p},\text{n})^{18}\text{F}$	$\text{H}_2^{18}\text{O}$ (98%)	12 $\mu\text{m}$ Titanium	50 $\mu\text{m}$ Havar®

**Table 3**  
Characteristics of the coils (given for one coil).

Inner diameter (cm)	Outer diameter (cm)	Height (cm)	Material	Weight (kg)
120	152.8	22	Copper, Epoxy	1218

into account as sources for secondary neutrons (target material plus windows). Each of these ports can be considered as individual “point-like” sources of secondary neutrons. Two types of target assemblies can be distinguished: those using liquid target materials, like for the production of  $^{18}\text{F}$  and  $^{13}\text{N}$ , and those using gaseous target materials, like for the production of  $^{11}\text{C}$ . The related schematics, as modelled in FLUKA, are shown in Fig. 2 and Fig. 3, respectively. The two target assemblies vary significantly by their geometry and the materials being used.

The 18 MeV proton beam was assumed to be pencil like. The interaction of the beam with the collimators was not taken into account because no detailed information on the beam emittance was available at these locations.

As described above, beam losses during acceleration are expected as an additional source for secondary neutrons. A simplified model for the beam loss mechanism was implemented in FLUKA for the calculation of the related neutron fluence. It is assumed here that 50% of the accelerated  $\text{H}^-$  beam particles are ionized by the residual gas inside the vacuum system. The stripping process in our simulation is uniformly distributed over the region of acceleration. The resulting H-atoms (ionization of  $\text{H}^-$ ) will tangentially continue their trajectories with a momentum  $p = qBr$ , where  $r$  is the radius of the trajectory at the stripping location,  $q$  the elementary charge and  $B$  the magnetic field. They will interact with the vacuum chamber, where neutrons are produced. Although the acceleration and stripping process was not simulated in detail, this simplified model reproduces the correct interaction rate of lost beam particles with the vacuum chamber. However, the real spatial distribution of the ionization processes could be different. Consequently, the energy spectrum of interacting particles may therefore deviate from what is assumed here as a first approximation. The properties of the target ports T1-T8 as secondary neutron sources are summarized in Table 4. The beam losses (BL) were added also to this list. For each of the nine sources, independent simulations were carried out in FLUKA taking into account the full geometry of the cyclotron.

A cylindrical coordinate system was defined for the scoring of the differential neutron fluence  $\Phi_i^s(E)$  from the sources  $s$  inside the sub volumes  $V_i$  of the magnetic coils as a function of the energy  $E$  in 260 bins (see Fig. 4). A scoring volume  $V_i$  can be identified by its coordinate  $(r, \phi, z)$ . In order to calculate the 3D-distribution, the volume of the coils was subdivided into 216 sub volumes with 24 different values in  $\phi$  and 3 different values in both  $r$  and  $z$ . For simplicity reasons, the pairs of discrete coordinates  $(r, z)$  were combined to positions  $P$ , as illustrated in Fig. 4. For each of the volumes  $V_i$ ,  $\Phi_i^s(E)$  originating from each of the sources  $s$  was recorded by FLUKA. The scoring volumes have sizes equivalent to 4–7 kg of copper. The azimuthal coordinate  $\phi = 0$  is defined by the centre of target T1. FLUKA also provides the statistical uncertainties of these calculations.

### 2.2.2. Estimation of the activation products and their activities

We calculated the activation products within the volumes  $V_i$  inside the magnet coils and their associated activities using ActiWiz 3.3, a software tool developed at CERN. The software makes it possible to quickly determine production rates and then calculate the activities of elementary or composite materials by using radiation fields with complex irradiation patterns. This two steps calculation is done analytically. An irradiation pattern is defined here as a sequence of consecutive periods of constant beam currents with periods without beam between (if required) and a cooling down period at the end. Thus, realistic irradiation scenarios with production cycles and variable beam currents can be

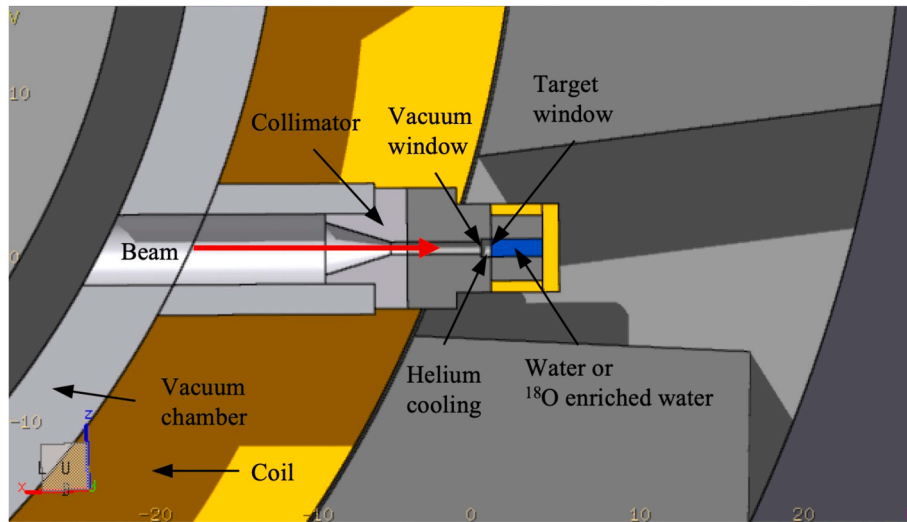


Fig. 2. Target assembly for the production of  $^{18}\text{F}$  or  $^{13}\text{N}$ . (For interpretation of the references to color in this figure legend, the reader is referred to the Web version of this article.)

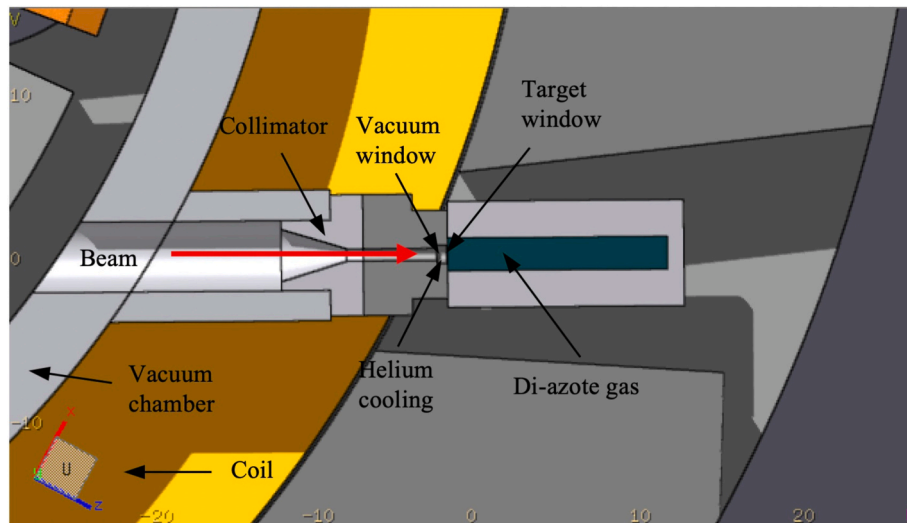


Fig. 3. Target assembly for the production of  $^{11}\text{C}$ . (For interpretation of the references to color in this figure legend, the reader is referred to the Web version of this article.)

Table 4

List of neutron sources taken into account for the simulation.

Source	Isotope	Target material used in FLUKA	Total protons
T1	$^{18}\text{F}$	$\text{H}_2^{18}\text{O}$	$1.83 \times 10^{21}$
T2	$^{18}\text{F}$	$\text{H}_2^{18}\text{O}$	$8.29 \times 10^{20}$
T3	Not used	–	0
T4	$^{11}\text{C}$	$\text{N}_2$ gas at 20 bars	$8.09 \times 10^{19}$
T5	$^{18}\text{F}$	$\text{H}_2^{18}\text{O}$	$9.81 \times 10^{19}$
T6	$^{18}\text{F}$	$\text{H}_2^{18}\text{O}$	$7.99 \times 10^{20}$
T7	$^{13}\text{N}$	$\text{H}_2\text{O}$	$1.16 \times 10^{20}$
T8	Not used	–	0
BL	–	Vacuum Chamber	$3.75 \times 10^{21}$

described. As an example, the irradiation pattern of target T1, as it was assumed for the calculation of the activation of the coils is given in Fig. 5. For a given volume  $V_i$  and a differential neutron fluence  $\Phi_i^s(E)$  from the source  $s$ , the ActiWiz calculations will return a list of the activated nuclides  $\{n_{i,j}^s\}$  with  $j \in [1, m_i^s]$  together with their corresponding specific activities  $a_{i,j}^s$  and uncertainties  $\Delta a_{i,j}^s$ .  $m_i^s$  is the number

of nuclides produced in the volume  $V_i$  by the source  $s$ . The result can be grouped together into activation tuples  $N_i^s$  containing  $m_i^s$  triplets with the information about the produced nuclides, their activities and uncertainties.

$$N_i^s = \left\{ \left( n_{i,1}^s, a_{i,1}^s, \Delta a_{i,1}^s \right), \dots, \left( n_{i,j}^s, a_{i,j}^s, \Delta a_{i,j}^s \right), \dots, \left( n_{i,m_i^s}^s, a_{i,m_i^s}^s, \Delta a_{i,m_i^s}^s \right) \right\} \quad (1)$$

The result for the total specific activities of the nuclides inside the volume  $V_i$  is obtained by summing over all sources:

$$N_i = \sum_s N_i^s = \left\{ \left( n_{i,1}, a_{i,1}, \Delta a_{i,1} \right), \dots, \left( n_{i,k}, a_{i,k}, \Delta a_{i,k} \right), \dots, \left( n_{i,m_i}, a_{i,m_i}, \Delta a_{i,m_i} \right) \right\} \quad (2)$$

, where  $\{n_{i,k}\} = \cup_s \{n_{i,j}^s\}$  is the union set of the nuclides produced by the different sources  $s$  in the volume  $V_i$  with  $k \in [1, m_i]$  and  $m_i$  is the corresponding number of nuclides. The activities and uncertainties simply result from:

$$a_{i,k} = \sum_s a_i^s(n_{i,k}) \quad (3)$$

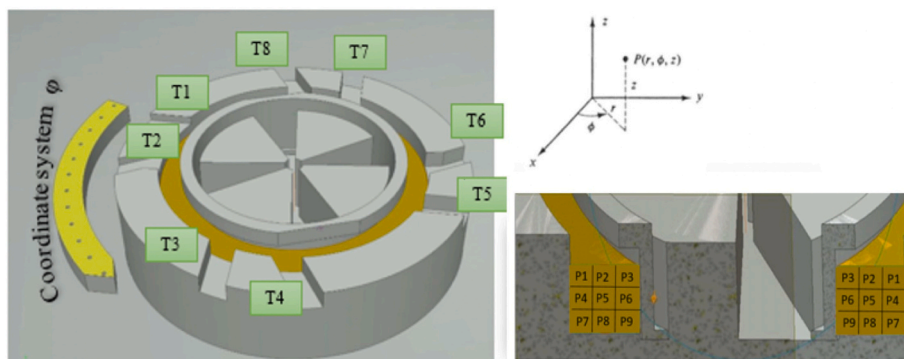


Fig. 4. Schematic view of the cyclotron showing the cylinder coordinates defined for the coils. The positions P1 to P9 are shown on the right. (For interpretation of the references to color in this figure legend, the reader is referred to the Web version of this article.)

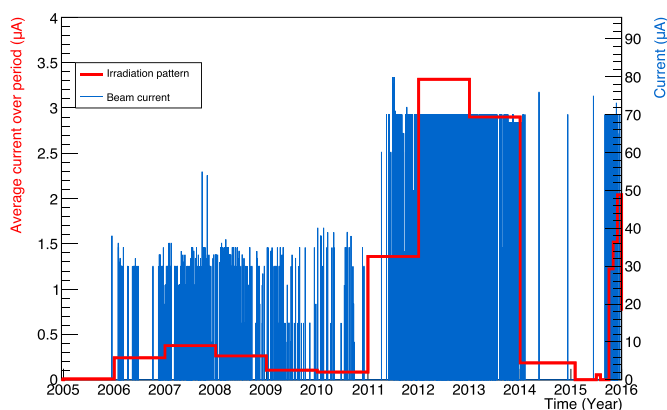


Fig. 5. Blue curve: beam current as a function of time. Red curve: average beam current per time interval (period). The period was set to one year for the years 2004–2014 and to one month for the year 2015. (For interpretation of the references to color in this figure legend, the reader is referred to the Web version of this article.)

$$\Delta a_{i,k} = \sqrt{\sum_s (\Delta a_i^s(n_{i,k}))^2} \quad (4)$$

The functions  $a_i^s(n_{i,k})$  and  $\Delta a_i^s(n_{i,k})$  return the activity and uncertainty of a nuclide  $n_{i,k}$  from  $N_i^s$ .

In order to facilitate the calculations, the software tool RAW was used, which permits to determine  $N_i$  in an automated way. In this study, both ActiWiz and RAW were applied for the first time for a low energy medical accelerator.

In summary,  $\Phi_i^s(E)$  are calculated with FLUKA,  $N_i^s$  are calculated in an automated way with RAW using ActiWiz, and finally  $N_i$  are calculated with RAW according to equation (2). RAW takes care of the handling of the input, intermediate and final data (fluence spectra, irradiation profiles and nuclide vectors) in a database. More information about RAW can be found in (Geyer et al., 2019).

### 2.3. Sampling and measurements of the coils

After removal from the cyclotron, the activated coils were placed in a secured waste storage area. Here, the distribution of count rates at the surface of the coils was measured with a bismuth germinate oxide detector (FHZ-512, Thermo Fisher). The measurements were taken every  $7.5^\circ$  in position P1 with a measurement time of 10 s each. The measurements were carried out at contact of the coils. The goal here is to make a qualitative comparison of the count rates at different locations. The resulting distribution indicates a strongly heterogeneous distribution of the activities inside the coils and shows two maxima around

$0^\circ$  close to T1 and T2 and around  $200^\circ$  close to T5 and T6. The corresponding azimuthal distribution is shown in Fig. 6. Due to the qualitative nature of this study, uncertainties are not discussed here. The background varied strongly with the position of measurement and originated to some extent from the coils themselves. A background correction has therefore not been applied.

Guided by this result, a set of 58 copper samples were extracted from the coil at different locations in  $\phi$  for the positions P1, P3, P7 and P9. The weights of the samples were in the range of 10–20 g each. The locations of the samples on the coil were determined with a precision of 1–2 cm. The samples were measured with a high purity germanium detector (HPGe). The measurement time was 1 h for all the samples with a dead time between 0.03% and 0.63%.

All samples showed a clear signal of the two gamma lines (1173 keV and 1332 keV) of  $^{60}\text{Co}$  in the spectrum. In addition,  $^{110\text{m}}\text{Ag}$  was identified in three samples. Most likely, the second signal comes from silver being an impurity in copper. A neutron activation analysis (NAA) estimated the weight fraction of silver in the copper coils to be  $2.2 \times 10^{-4}$ . In addition to the statistical uncertainties, the systematic uncertainties of the spectroscopy results were estimated as 15%. The precision is limited by the geometrical model for the calculation of the detection efficiencies. The detection efficiencies were estimated with the help of LabSOCS, a calibration software from Mirion Technologies, Inc. (MIRION, 2017). The drilling chips of the samples have been collected in plastic bags. The bags have been measured in a distance of a few millimetres to the detector, in order to get a low MDA (minimum detectable activity) in a reasonable measurement time. The samples were described as simplified rectangular boxes as an approximation of the bags filled with these chips. Cascade summing corrections were applied for  $^{60}\text{Co}$ .

## 3. Results

We characterised the magnet coils of the cyclotron by applying the materials and methods described above. Our first step involved studying the properties of the target assemblies as sources for secondary neutrons. The results are summarized below. We then discuss the activation process of the hotspot of the coils close to T1 based on the simulation results and we give the azimuthal distribution of the relevant activation products for the position P1. Next, we compare the simulation results to those of spectrometry measurements and follow with a discussion of uncertainties. Finally, we present the results of the characterisation of the coils for all 216 scoring volumes defined above. Unless otherwise stated, in the following we provide the uncertainties for one standard deviation.

### 3.1. Characterisation of the target assembly components as neutron sources

Using FLUKA, we first studied the number of emitted neutrons as a function of energy by the components, which are hit by the full beam

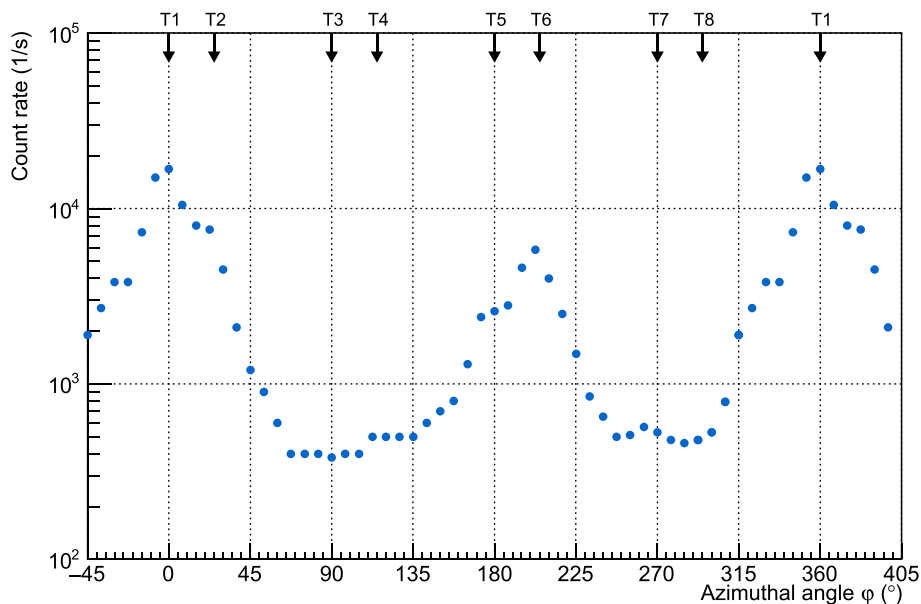


Fig. 6. Azimuthal distribution of the BGO count rates measured at position P1. T1-T8 denotes for the target positions. The hotspot of the coils is at zero degrees next to the target T1. In order to illustrate the distribution around the hotspot, the distribution has been cyclically expanded below 0 and above 360°.

intensity. These are the three different production-materials ( $H_2^{18}O$ ,  $H_2O$  and  $N_2$ ) used for the production of  $^{18}F$ ,  $^{13}N$  and  $^{11}C$ , the target windows, the vacuum windows and the stripper foils. The simulations assume an 18 MeV pencil like proton beam. The individual components listed above are simulated with their real dimensions. Other components of the target assembly or cyclotron were omitted from the simulation in order to avoid secondary processes. The results are shown in Fig. 7. The strongest emitter of neutrons is the material for the  $^{18}F$  production. The neutrons mainly come from the reaction  $^{18}O(p,n)^{18}F$ . The target material for  $^{11}C$  produces around ten times less neutrons, followed by the target and vacuum windows. The target material for the production of  $^{13}N$  creates one thousand times less neutrons compared to the target material for  $^{18}F$  production over the entire energy range. The production of neutrons in that target assembly is dominated by the windows. Thermal neutrons are not necessarily produced by the primary

interactions of the proton beam. Like in the example of the target material  $H_2^{18}O$  for the production of  $^{18}F$ , they are generated by secondary interactions of neutrons within the production material.

The yield of secondary neutrons can then be classified from highest to lowest as follows:

1.  $H_2^{18}O$  for the production of  $^{18}F$ ;
2.  $N_2$  for the production of  $^{11}C$ ;
3. The target window of the  $^{11}C$  target assembly (500  $\mu m$  Al);
4. The target window of the  $^{18}F$  target assembly (50  $\mu m$  Havar);
5. The target window of the  $^{13}N$  target assembly (25  $\mu m$  Havar);
6. The vacuum window (12.5  $\mu m$  Ti);
7.  $H_2O$  for the production of  $^{13}N$ ;
8. The stripper foils (5  $\mu m$  C).

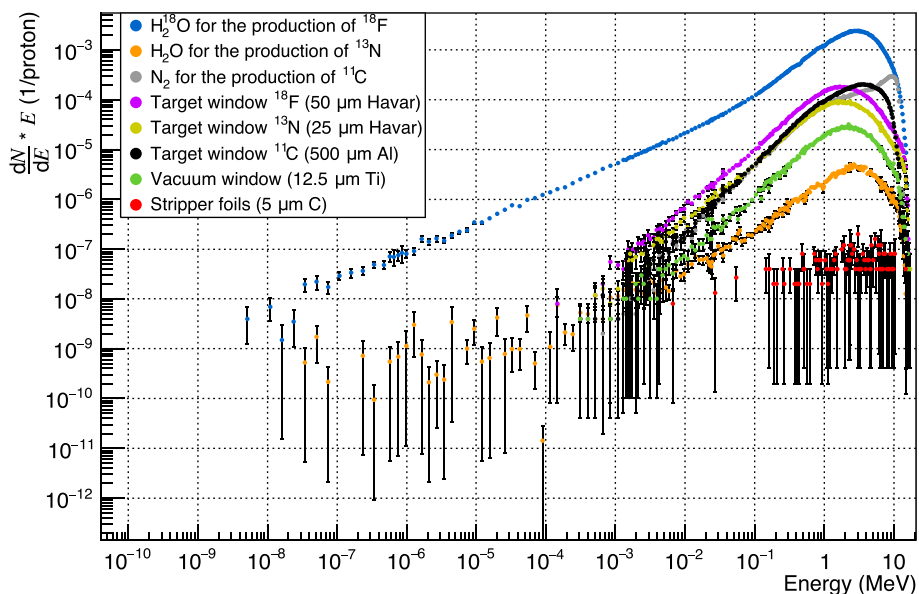


Fig. 7. Neutron energy spectra per primary proton emitted by the different components. The error bars represent the statistical uncertainties of the FLUKA calculations. (For interpretation of the references to color in this figure legend, the reader is referred to the Web version of this article.)

In order to crosscheck the correctness of the FLUKA calculations, we compared the production yields for  $^{18}\text{F}$ ,  $^{13}\text{N}$  and  $^{11}\text{C}$  with values from the IAEA database for medical radioisotope production (IAEA, 2018). The results are given in Table 5. The values agree within a few percent for  $^{18}\text{F}$  and the ratio FLUKA/IAEA is compatible with the results from the study of (Infantino et al., 2015). Larger deviations were observed for  $^{13}\text{N}$  and  $^{11}\text{C}$ . This gives a first idea on the uncertainties of the FLUKA calculations.

### 3.2. Characterisation of the hotspot of the coils by simulation

As already mentioned, the hotspot of the coil is next to the target T1, the target assembly for the  $^{18}\text{F}$  production with the highest integrated beam current. The corresponding scoring volume for the FLUKA calculations is denoted by  $V_1$  (see also 2.2.1) and has the coordinates ( $\phi = 0$ ,  $P = P1$ ). Fig. 8 shows the differential neutron fluence  $\Phi_s^d(E)$  at this location for the different neutron sources  $s$ . Obviously, the main contribution comes from target T1, which is the closest.

The nuclide content  $N_1$  of the hotspot  $V_1$  was then calculated using Equation (2) with the appropriate irradiation profiles and differential neutron fluence spectra as input for ActiWiz. We assumed that the coils are made from pure copper with an impurity of 0.022% silver. The results are given in Table 6 for cooling times after irradiation of 1 day and 2.5 years, respectively. The statistical uncertainties of the ActiWiz calculations were below 1% for all the radionuclides.

Following the example above, we then determined the nuclide contents  $N_i$  for all the 216 sub volumes  $V_i$ , where the differential neutron fluence was recorded as described in section 2.2.1. In Fig. 9, the specific activities caused by the neutron fluence from target T1 are compared with the total specific activities obtained by Equation (2) as a function of  $\phi$ . The results are given for the position P1 for a cooling time of 2.5 years. The only radiologically relevant radionuclides were  $^{60}\text{Co}$ ,  $^{63}\text{Ni}$  and  $^{110\text{m}}\text{Ag}$ .

The specific activities of  $^{63}\text{Ni}$  vary between 0.5 Bq/g and 100 Bq/g and those of  $^{60}\text{Co}$  between 0.1 Bq/g and 20 Bq/g. The specific activities of  $^{110\text{m}}\text{Ag}$ , which were omitted from the plot for clarity reasons, are in the range of  $5.10^{-3}$  Bq/g and 0.2 Bq/g. The activation distributions are strongly modulated by the targets. As can be seen in Fig. 9, the activation of the coil close to target T1 is dominated by this target. In larger distances, the contribution of other targets becomes clearly relevant. They must be taken into account following Equation (2).

### 3.3. 3-D distribution of activation and comparison with measurements

To compare the measured results with the simulations, we defined scoring volumes at 144 different equidistant azimuth angles  $\phi$  and at four different positions (P1, P3, P7 and P9). The sizes of the scoring volumes were around  $10\text{ cm}^3$  and were comparable to those of the spectroscopy samples. We compared the measurements with the simulation for a cooling time of 2.5 years. This time corresponds to the moment when the characterisation started.

The expectations for the specific activity of  $^{60}\text{Co}$  from the simulation are shown in Fig. 10. The summed contributions from the targets T1 - T8 are plotted separately from those from beam losses BL inside the machine. As already mentioned, we assumed 50% losses during acceleration, a typical value quoted for this type of accelerator (Papash and

**Table 5**

Comparison of the activities expected by FLUKA with those expected by IAEA. The activities are given after 1 h of irradiation with a beam current of  $1\ \mu\text{A}$ .

Radionuclides	Activity FLUKA (GBq)	Activity IAEA (GBq)	FLUKA/IAEA
$^{18}\text{F}$	4.15	4.29	0.97
$^{13}\text{N}$	1.97	1.64	1.20
$^{11}\text{C}$	7.98	5.51	1.45

Alenitsky, 2008). The plot clearly shows that the activation of the coils is dominated by the production targets. Beam losses contributed only in parts of lowest activation of the coils. Fig. 10 also shows the spectroscopy results of the material samples. The measured specific activities inside the coils varied by more than four orders of magnitudes between 0.03 Bq/g and 100 Bq/g. A first comparison between measurements and simulation shows that the latter systematically underestimates the activation of the coils by about a factor 2.5. This underestimation seems to be uniform and relatively independent of the position inside the coils in both  $\phi$  and  $P$ . In order to improve the precision of the simulation predictions, we then multiplied the beam currents used for the irradiation profiles by a correction factor of 2.5.

After normalisation by this factor, the simulation showed a good agreement with measurements, as can be seen in Fig. 11. Fig. 12 shows the distribution of  $(a^{\text{meas}} - a^{\text{sim}})/a^{\text{sim}}$ . Under the assumption that the uncertainties of the spectrometry measurements are small compared to those of the simulation, this distribution directly reflects the (experimentally determined) uncertainties of the simulation results, including those listed in Table 7. The 58 samples, which were used for the comparison, cover a large part of the surface of the coils. Based on this histogram, the uncertainties on the activity of  $^{60}\text{Co}$  were estimated to  $[-60\% + 100\%]$  at a confidence level of 95% over the full volume of the coils. For the characterisation of the coils, which is described in the next section, we assumed the same uncertainty for the radionuclides  $^{63}\text{Ni}$  and  $^{110\text{m}}\text{Ag}$ .

In order to explain the correction factor, we conducted several systematic studies for the hotspot. As shown in section 3.1, the production of  $^{18}\text{F}$  is correctly described by the simulation. This reaction channel  $^{18}\text{O}(p,n)^{18}\text{F}$  was the main source of secondary neutrons next to the hotspot. Although the total production seems to be right, the anisotropy of emitted neutrons could still be different between simulation and reality. The activation of the hotspot is dominated by neutrons emitted in backward direction of the target cell. In a publication from (Hagiwara et al., 2011), the experimental data on the energy spectra and angular distributions for neutrons is compared with Monte-Carlo calculations (MCNPX (Pelowitz, 2011) and PHITS (Sato et al., 2018)) for proton energies of 18 MeV. Significant discrepancies have been observed between experimental data and simulation results, depending on the neutron energy and emission angle. A very recent article (Bakhtiari et al., 2020) compares the same experimental data with FLUKA simulations. According to their results, the emission of neutrons in backward direction ( $150^\circ$ ) is underestimated by a factor of two or more in the energy range between 6 and 11 MeV by the simulation. This range is absolutely relevant for the production of  $^{60}\text{Co}$  in copper. It could explain at least a part of the correction factor.

Beside the targets, also the collimators may be hit by the beam. Twenty percent of the beam interactions inside the collimator of the target T1 would contribute only to an additional three percent in activity of  $^{60}\text{Co}$ . The uncertainties of other sources are summarized in Table 7.

For the calculation of the activation of the copper of the coils, we assumed the average density of  $7.87\text{ g/cm}^3$  of the material, while the density of pure copper is  $8.94\text{ g/cm}^3$ . The difference comes mainly from epoxide and a cooling flask inside the coils. These materials were not explicitly included in our geometrical description in FLUKA. The necessary technical details were not available. In order to estimate an impact of different density assumptions on the activation in the surrounding of the hotspot, we compared the simulation results for  $^{60}\text{Co}$  for both densities. They differ by 10% and cannot explain the necessary correction factor here.

The position of the target assembly T1 relative to the coils is known with a precision of about 1 cm. When varying this position in the simulation by that quantity, the  $^{60}\text{Co}$  activity changed by 10% for the hotspot and even less for locations further away from T1.

The coordinates of the samples have an uncertainty of 1–2 cm. Because of the large gradients of the activity distribution, this had the biggest impact on the uncertainties, which may become 40% in certain

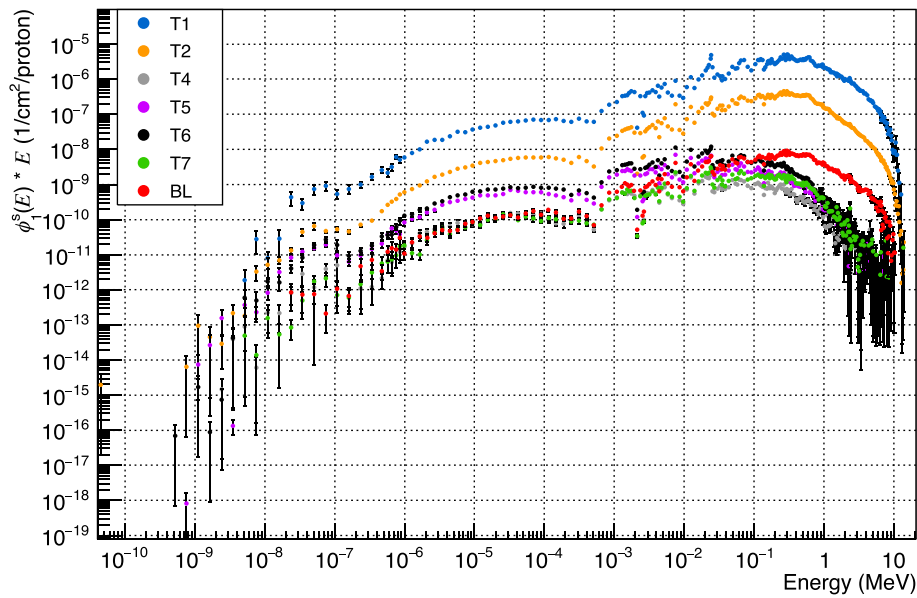


**Fig. 8.** Neutron fluence at the location of the hotspot of the coils. The contributions from each source are shown separately. The error bars represent the statistical uncertainties of the FLUKA calculations. (For interpretation of the references to color in this figure legend, the reader is referred to the Web version of this article.)

**Table 6**

Radionuclides and corresponding activities for 1 day and 2.5 years of cooling. Only nuclides with specific activities larger  $10^{-3}$  Bq/g are listed.

1 day of cooling		
Isotope	$T_{1/2}$ (y)	$a_1$ (Bq/g)
$^{64}\text{Cu}$	$1.45 \times 10^{-3}$	$7.1 \times 10^3$
$^{63}\text{Ni}$	$1.01 \times 10^2$	$8.5 \times 10^1$
$^{60}\text{Co}$	5.27	$1.9 \times 10^1$
$^{110\text{m}}\text{Ag}$	$6.84 \times 10^{-1}$	2.4
$^{110}\text{Ag}$	$7.78 \times 10^{-7}$	$3.3 \times 10^{-2}$
$^{65}\text{Ni}$	$2.87 \times 10^{-4}$	$1.2 \times 10^{-2}$
$^{108\text{m}}\text{Ag}$	$4.18 \times 10^2$	$8.5 \times 10^{-3}$
2.5 years of cooling		
Isotope	$T_{1/2}$ (y)	$a_1$ (Bq/g)
$^{63}\text{Ni}$	$1.01 \times 10^2$	$8.4 \times 10^1$
$^{60}\text{Co}$	5.27	$1.4 \times 10^1$
$^{110\text{m}}\text{Ag}$	$6.84 \times 10^{-1}$	$1.9 \times 10^{-1}$
$^{108\text{m}}\text{Ag}$	$4.18 \times 10^2$	$8.5 \times 10^{-3}$

regions of the coil.

Unfortunately, we have no reliable information about the uncertainties of the beam currents.

$^{60}\text{Co}$  is produced inside the coils via the reaction  $^{63}\text{Cu}(n,\alpha)^{60}\text{Co}$ . Both software tools, FLUKA and ActiWiz, rely on the same cross section data. In order to validate the correctness of the ActiWiz calculations at low energies, a direct comparison between FLUKA and ActiWiz has been made. The comparison is based on the calculation of the activation products inside three volumes  $V_1$ ,  $V_4$  and  $V_{17}$  from source T1. The irradiation pattern from Fig. 5 and a cooling time of 2.5 years were assumed. The results are summarized in Table 8. For  $^{60}\text{Co}$  and  $^{63}\text{Ni}$ , the results agree within uncertainties. The values for  $^{110\text{m}}\text{Ag}$  differ significantly between ActiWiz and FLUKA. While the calculation of ActiWiz is based on the  $^{109}\text{Ag}(n,\gamma)^{110\text{m}}\text{Ag}$  cross section taken from the JEFF-3.1 nuclear data library, FLUKA (version3.0) assumes an arbitrary production rate of 50% relative to all produced  $^{110}\text{Ag}$  states.

In general, the uncertainties of ActiWiz are an order of magnitude lower compared to FLUKA. This advantage results from the analytical calculation of the activities from the fluence spectra compared to the pure Monte-Carlo approach in FLUKA.

The operation between 2000 and 2005 was not taken into account in our calculations because no operational data has been available. Assuming working conditions similar to the last years, the  $^{60}\text{Co}$  activities would increase by about 15% and the  $^{63}\text{Ni}$  about 30%.

An unambiguous explanation for the correction factor is still missing. Further investigations would be necessary. However, what counts for the characterisation is a reasonable agreement between the measurements and the simulation. This was the case after we applied the correction factor.

### 3.4. Radiological characterisation of the coils

According to Art.106 of the Swiss radiation protection ordinance (ORaP) (The Swiss federal council, 2019), a material is classified as radioactive if one of the following criteria is fulfilled:

1. The surface contamination exceeds the surface contamination limits CS.
2. The dose rate after background suppression exceeds  $0.1 \mu\text{Sv/h}$  at 10 cm of distance.
3. The specific and absolute activity of the radionuclide exceeds the clearance limits LL.

Contamination is rarely an issue with this type of accelerator. Our study confirmed this by negative wipe tests on the coils. Accordingly, this work focused on determining the activation products within the irradiated material (criterion 3). The values of LL are specified in Annex 3 Column 9 of the ORaP. If a material contains more than one radionuclide, the following summation rule has to be applied for the criterion 3:

$$S_{LL} = \sum_{l=1}^m \frac{a_l}{LL_l} \quad (5)$$

Here,  $a_l$  denotes the specific activity and  $LL_l$  denotes the clearance limits for each radionuclide  $l$ .

In case of homogenisation of the coil by melting, equation (5) becomes:

$$S_{LL,h} = \sum_{l=1}^m \frac{\bar{a}_l}{LL_l} = \sum_{l=1}^m \frac{A_l/M}{LL_l} \quad (6)$$

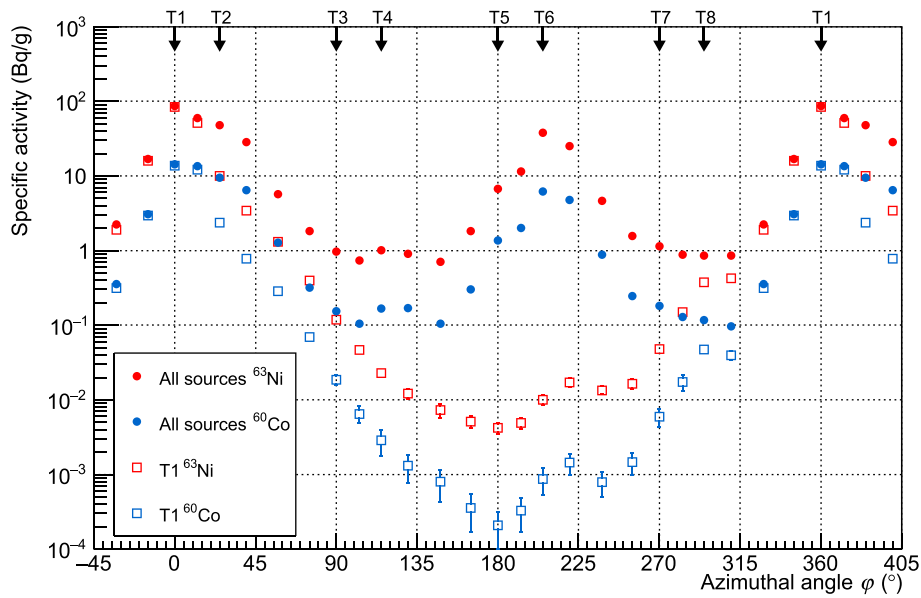


Fig. 9. Azimuthal distribution of the specific activities of  $^{60}\text{Co}$  and  $^{63}\text{Ni}$  for position P1 for a cooling time of 2.5 years. The error bars represent the statistical uncertainties of the ActiWiz calculations. (For interpretation of the references to color in this figure legend, the reader is referred to the Web version of this article.)

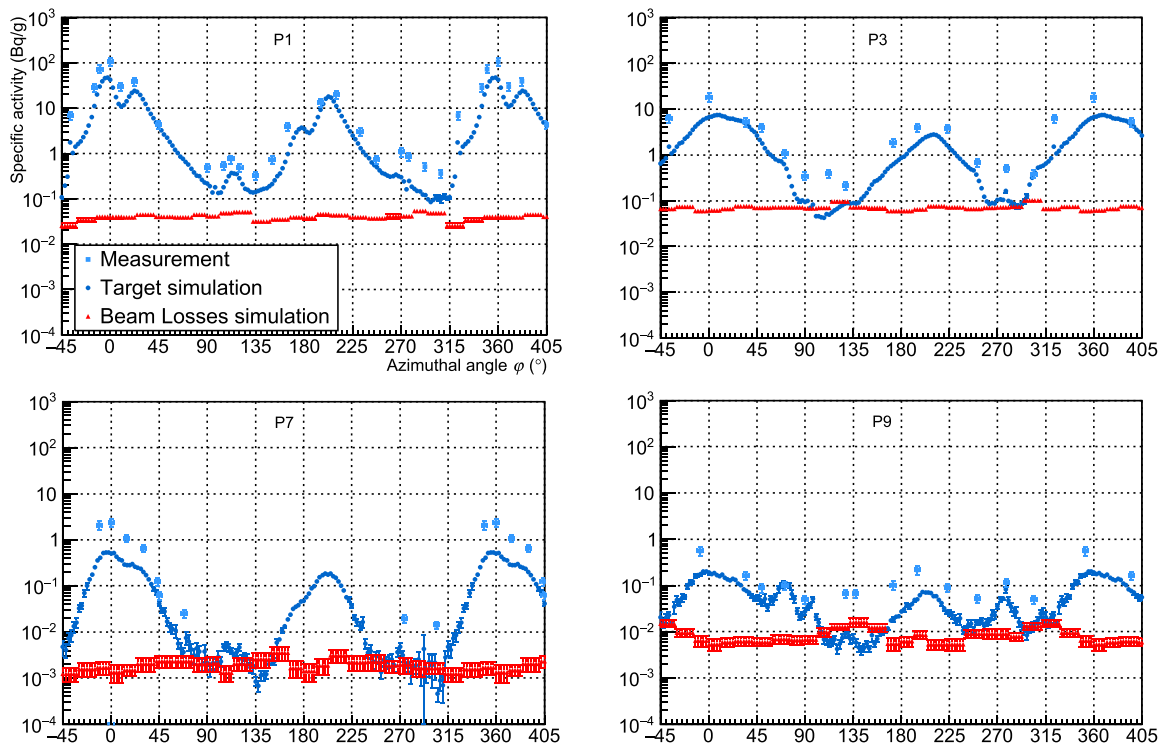


Fig. 10. Azimuthal distribution of the specific activities of  $^{60}\text{Co}$  for the positions P1, P3, P7, and P9. Simulation results are compared to measurements. The contributions from targets and beam losses are plotted separately for the simulation. (For interpretation of the references to color in this figure legend, the reader is referred to the Web version of this article.)

, where  $\bar{a}_i$  are the specific activities of the activation products after homogenisation and  $A_l$  are the absolute activities and  $M$  the total mass of the coils.

The list of radionuclides  $\{n_l\}$  with  $l \in [1, m]$ , which have been produced inside the coils, can simply be extracted from the activation tuple  $N_i$  (see also equation (2)) as the union set of nuclides from each volume  $V_i : \{n_l\} = \cup_i \{n_{i,k}\}$ . The total activity  $A_l$  is then calculated with the equation:

$$A_l = \sum_{i=1}^{216} a_i(n_l) * w_i \tag{7}$$

, where the function  $a_i(n_l)$  extracts the specific activity of the nuclide  $n_l$  inside the volume  $V_i$  from  $N_i$  and  $w_i$  denotes the mass of the volume  $V_i$ .

In order to determine which part of the copper coils satisfies the clearance criterion, we plotted the three-dimensional distribution of  $S_{LL}$ ,

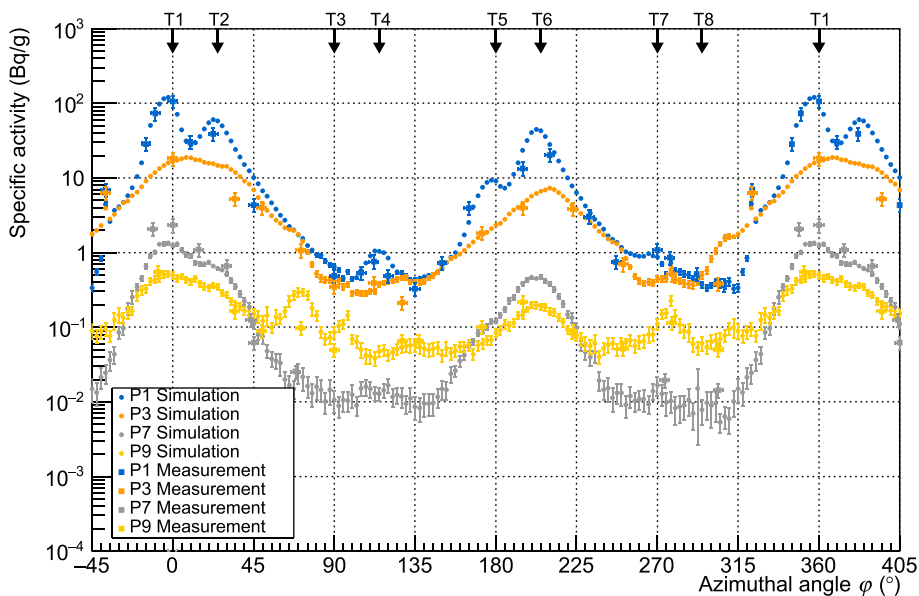


Fig. 11. Simulated azimuthal distribution of the specific activities of <sup>60</sup>Co after normalisation in comparison with measurements. (For interpretation of the references to color in this figure legend, the reader is referred to the Web version of this article.)

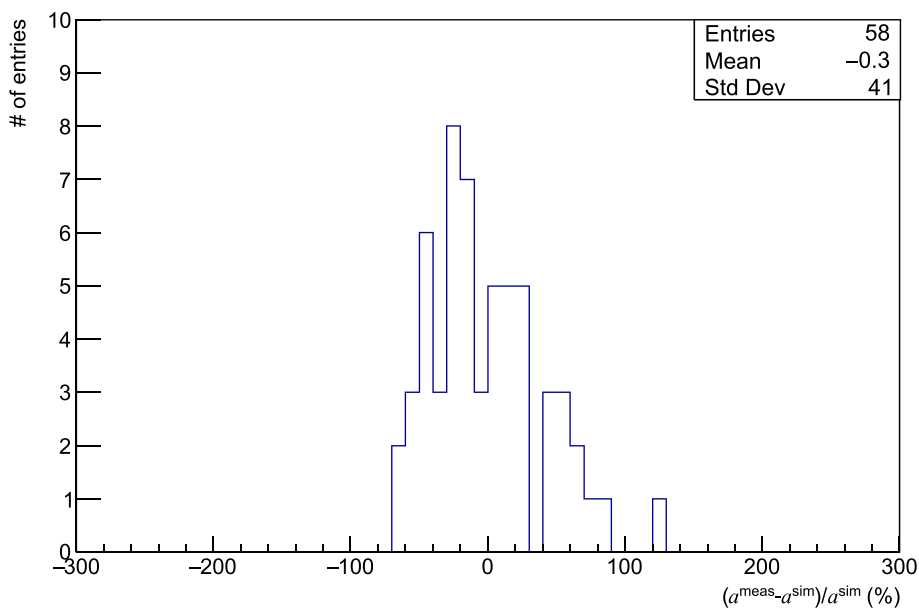


Fig. 12. Distribution of  $(a^{meas} - a^{sim})/a^{sim}$  for <sup>60</sup>Co after normalisation.

Table 7

Sources of uncertainties for the simulated and measured activities of <sup>60</sup>Co.

Source	Uncertainty (max)
Spectrometry	15%
Magnet density FLUKA	10%
Position of the target assemblies relative to the coils	10%
Coordinates of samples	40%

as calculated from  $N_i$  (see Equation (2)) after normalisation, for a cooling time of two and a half years in Fig. 13. In Switzerland, a cooling time of 30 years is required if the material can be cleared afterwards (see Art.117 of the ORaP). The result for a cooling time of 30 years is given in Fig. 14. The size of the volumes used for these calculations corresponds to those defined in section 2.2.1. After two and a half years of cooling,

$72^{+18}_{-20}$  % of the coil volume is considered radioactive in terms of  $S_{LL} > 1$  (Fig. 13).

If the activity distribution of the coils were homogenised by melting, the activity of the copper would result to  $S_{LL,h} = 20^{+9}_{-6}$ . The material could therefore not be cleared.

After 30 years of cooling, only  $15^{+8}_{-11}$  % of the volumes are still considered radioactive and  $85^{+11}_{-8}$  % of the volumes could be released. After homogenisation,  $S_{LL,h}$  would decrease approximately to  $S_{LL} = 0.6^{+0.3}_{-0.2}$ . In that case, the entire material could be recycled.

Here, the values of  $S_{LL}$  are given at a confidence level of 95%. The uncertainties defined in the previous section were quadratically propagated. The uncertainties of the spectroscopy measurements were taken into account.

The total activities A, the mean specific activities  $\bar{a}$  and  $S_{LL,h}$  after homogenisation are summarized in Table 9 for the relevant

**Table 8**

Comparison of specific activities calculated by FLUKA and ActiWiz for the irradiation pattern shown in Fig. 5 and a cooling time of 2.5 years (the uncertainties are given for one standard deviation).

Volume	Radionuclide	Activity (Bq/g) FLUKA	Activity (Bq/g) ActiWiz
V <sub>1</sub>	<sup>60</sup> Co	$3.69 \times 10^1 \pm 6.35$	$4.09 \times 10^1 \pm 3.2 \times 10^{-1}$
	<sup>63</sup> Ni	$1.65 \times 10^2 \pm 3.30$	$1.63 \times 10^2 \pm 3.6 \times 10^{-1}$
	<sup>110m</sup> Ag	$1.45 \pm 3.12 \times 10^{-1}$	$5.78 \times 10^{-2} \pm 2.05 \times 10^{-3}$
V <sub>4</sub>	<sup>60</sup> Co	$1 \times 10^1 \pm 3.07$	$9.04 \pm 1.42 \times 10^{-1}$
	<sup>63</sup> Ni	$3.87 \times 10^1 \pm 1.78$	$3.71 \times 10^1 \pm 1.5 \times 10^{-1}$
	<sup>110m</sup> Ag	$1.36 \pm 2.89 \times 10^{-1}$	$3.99 \times 10^{-2} \pm 1.66 \times 10^{-3}$
V <sub>17</sub>	<sup>60</sup> Co	$1.63 \pm 1.12$	$1.22 \pm 5.64 \times 10^{-2}$
	<sup>63</sup> Ni	$3.97 \pm 6.04 \times 10^{-1}$	$4.64 \pm 5.9 \times 10^{-2}$
	<sup>110m</sup> Ag	$2.82 \times 10^{-1} \pm 1.22 \times 10^{-1}$	$1.41 \times 10^{-2} \pm 1.02 \times 10^{-3}$

radionuclides and for cooling times of 2.5 years and 30 years.

These results can be used by the local radiation protection officer and the authorities to identify the appropriate waste management procedure for the coils.

#### 4. Conclusion

We radiologically characterised a major component (here the magnet coils) of a biomedical cyclotron by determining the three-dimensional distribution of activities of all relevant activation products. In order to obtain a complete picture of these distributions, we combined the results of  $\gamma$ -ray measurements of material samples of the coils with the expectations from a Monte-Carlo simulation. FLUKA, ActiWiz and RAW were used for the simulation calculations. The latter two are new software tools developed at CERN. They were used here for the first time in a medical environment for low energy accelerators in the range of MeV. These tools were essential in that they enabled us to obtain detailed results with reasonable computing time and in an efficient way. ActiWiz calculates the activities of activation products analytically, which helps to keep the uncertainties small compared to a pure Monte-Carlo approach like FLUKA. In addition, ActiWiz uses the corresponding production cross-section for <sup>110m</sup>Ag, which is another advantage when compared with FLUKA (version 3.0). We then used the spectroscopy measurements of samples to identify the relevant sources

of secondary neutrons and to validate the assumptions made by the simulation model. This study determined that the strongest sources of secondary neutrons are the production targets for <sup>18</sup>F. Nevertheless, in regions with low activation of the coils, we were able to determine the contributions from other sources, like beam losses or target windows, in order to make a complete description of the activity distributions by the model.

It was necessary to apply a correction factor on the simulation data to obtain a good agreement between simulation and measurements results. This factor seems to be uniform and relatively independent of the location inside the coils. Once applied, both measurement and simulation results showed a good agreement considering that the activities vary by more than four orders of magnitude within the coils. Presently, the reasons for the required correction are not fully understood. They should be further investigated. In a recent article (Bakhtiari et al., 2020), a comparison of the FLUKA results for the angular distribution of emitted neutrons from the <sup>18</sup>O(p,n)<sup>18</sup>F reaction with experimental data suggests that the neutron fluence inside the coils by our simulation could be underestimated. If confirmed, an improvement of the underlying simulation models would of course be desirable.

We assumed that the coils are made from pure copper with some silver as impurity. Because of the high purity of the material (>99.96%) and our observations, we presently have no evidence for additional relevant impurities. Nevertheless, a detailed chemical analysis of the copper material would be preferable to remove any doubts.

Our results made it possible to characterise the coils radiologically. After 2.5 years of cooling, the biggest part of the coils must be classified as radioactive. However, after 30 years, more than 85% of the material could be cleared. After homogenisation, all material could be recycled. Based on these results, the local radiation protection officer and the authorities can identify the appropriate way of waste management for the coils.

The methods applied here are well suited for providing similar detailed information about the activity distributions of other components of the accelerator or its environment.

#### CRediT authorship contribution statement

**V. Bonvin:** Writing - original draft, Visualization, Methodology, Software, Investigation. **F. Bochud:** Resources, Supervision, Investigation. **J. Damet:** Resources, Project administration, Conceptualization. **C.**

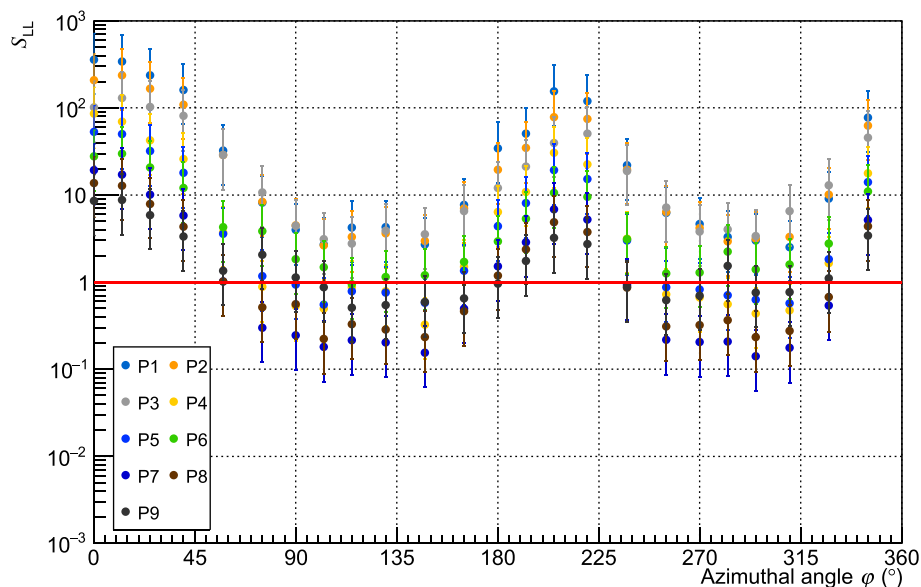


**Fig. 13.** Azimuthal distribution of  $S_{LL}$  after 2.5 years of cooling. Volumes with  $S_{LL}$  larger than one count as radioactive (points above the red line). Error bars are given at a confidence level of 95%. (For interpretation of the references to color in this figure legend, the reader is referred to the Web version of this article.)

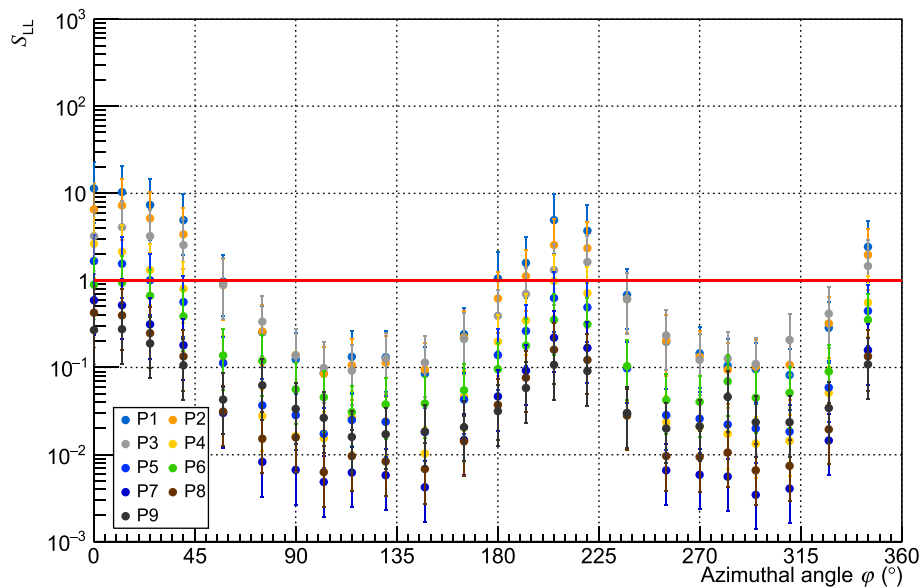


Fig. 14. Azimuthal distribution of  $S_{LL}$  after 30 years of cooling. Volumes with  $S_{LL}$  larger than one count as radioactive (points above the red line). Error bars are given at a confidence level of 95%. (For interpretation of the references to color in this figure legend, the reader is referred to the Web version of this article.)

Table 9

Total activities, mean specific activities and summation values after homogenisation for each of the coils.

2.5 years of cooling				
Radionuclides	A (MBq)	$\bar{a}$ (Bq/g)	LL (Bq/g)	$S_{LL,h}$
$^{63}\text{Ni}$	13.4	11.0	100	$20_{-6}^{+9}$
$^{60}\text{Co}$	2.3	1.9	0.1	
$^{110m}\text{Ag}$	$1.5 \times 10^{-2}$	$1.2 \times 10^{-2}$	0.1	
30 years of cooling				
Radionuclides	A (MBq)	$\bar{a}$ (Bq/g)	LL (Bq/g)	$S_{LL,h}$
$^{63}\text{Ni}$	11.1	9.1	100	$0.6_{-0.2}^{+0.3}$
$^{60}\text{Co}$	$6.3 \times 10^{-2}$	$5.1 \times 10^{-2}$	0.1	
$^{110m}\text{Ag}$	$1.2 \times 10^{-14}$	$1.0 \times 10^{-14}$	0.1	

**Theis:** Writing - review & editing, Conceptualization, Methodology, Software, Investigation, Validation, Data curation, Supervision. **H. Vincke:** Conceptualization, Methodology, Software, Validation. **R. Geyer:** Conceptualization, Methodology, Software, Validation, Supervision, Funding acquisition.

#### Declaration of competing interest

The authors declare that they have no known competing financial interests or personal relationships that could have appeared to influence the work reported in this paper.

#### Acknowledgements

The authors would like to thank Jean-Michel Geets and Rachid Ayad from the company IBA for the various documents and information about the cyclotron. We would also like to thank Nicolas Cherbuin for his help with taking samples.

#### References

- Bakhtiari, M., Mokhtari Oranj, L., Jung, N.-S., Lee, A., Lee, H.-S., 2020. Estimation of neutron production yields from H2180 as the 18F-production target bombarded by 18-MeV protons. *Radiat. Phys. Chem.* 177, 109120. <https://doi.org/10.1016/j.radphyschem.2020.109120>.
- Böhlen, T.T., Cerutti, F., Chin, M.P.W., Fassò, A., Ferrari, A., Ortega, P.G., Mairani, A., Sala, P.R., Smirnov, G., Vlachoudis, V., 2014. The FLUKA code: developments and challenges for high energy and medical applications. *Nucl. Data Sheets* 120, 211–214. <https://doi.org/10.1016/j.nds.2014.07.049>.
- Braccini, S., 2016. Compact medical cyclotrons and their use for radioisotope production and multi-disciplinary research. In: *Proceedings of Cyclotron 2016. Zurich, Switzerland*, p. 232.
- Calandrino, R., del Vecchio, A., Savi, A., Todde, S., Griffoni, V., Brambilla, S., Parisi, R., Simone, G., Fazio, F., 2006. Decommissioning procedures for an 11 MEV self-shielded medical cyclotron after 16 years OF working time. *Health Phys.* 90, 588–596. <https://doi.org/10.1097/01.HP.0000190161.96172.ae>.
- Eurostat, 2019. *Healthcare Resource Statistics - Technical Resources and Medical Technology. Statistics Explained*.
- Ferrari, A., Sala, P.R., Fassò, A., Ranft, J., 2005. Fluka : a multi-particle transport code (No. SLAC-R-773, 877507). <https://doi.org/10.2172/877507>.
- Geyer, R., Damet, J., Theis, C., Vincke, H., Sotiropoulou, M., Bonvin, V., 2019. *Radiological Characterization of Activated Material at Accelerators. Presented at the IRPA 2018, The Hague, Netherlands*, pp. 6–13.
- Hagiwara, M., Sanami, T., Masumoto, K., Iwamoto, Y., Matsuda, N., Sakamoto, Y., Nakane, Y., Nakashima, H., Uwamino, Y., 2011. Spectrum measurement of neutrons and gamma-rays from thick H1820 target bombarded with 18 MeV protons. *J. Kor. Phys. Soc.* 59, 2035–2038. <https://doi.org/10.3938/jkps.59.2035>.
- IAEA, 2019. *Cyclotrons used for radionuclide production*. <https://nucleus.iaea.org/sites/accelerators/Pages/Cyclotron.aspx> accessed 01 January 2020.
- IAEA, 2018. *Charged-particle cross section database for medical radioisotopes production*. [https://www-nds.iaea.org/medical/positron\\_emitters.html](https://www-nds.iaea.org/medical/positron_emitters.html) accessed 31 January 2020.
- IAEA, 2009. *Cyclotron Produced Radionuclides: Principles and Practice Technical*. IAEA, 2003. *Decommissioning of Small Medical, Industrial and Research Facilities*. IBA, 2009. *Cyclone 18/9*.
- Infantino, A., Marengo, M., Baschetti, S., Ciorica, G., Longo Vaschetto, V., Luccioni, G., Massucci, P., Vichi, S., Zagni, F., Mostacci, D., 2015. Accurate Monte Carlo modeling of cyclotrons for optimization of shielding and activation calculations in the biomedical field. *Radiation Physics and Chemistry, Proceedings of the 9th International Topical Meeting on Industrial Radiation and Radioisotope Measurement Applications* 116, 231–236. <https://doi.org/10.1016/j.radphyschem.2015.01.001>.
- MIRION, 2017. *LabSOCS calibration software*. <https://www.mirion.com/products/labsocs-calibration-software> accessed 10 September 2020.
- NEA, 2013. *Radiological Characterisation for Decommissioning of Nuclear Installations (No. NEA/RWM/WPDD(2013)2)*.
- Papash, A.I., Alenitsky, Yu.G., 2008. On beam intensity upgrade in the commercial cyclotrons of negative hydrogen ions. *Phys. Part. Nucl. Lett.* 5, 469–472. <https://doi.org/10.1134/S1547477108050117>.

- Pelowitz, D.B., 2011. MCNPX Users Manual Version 2.7.0 (No. LA-CP-11-00438).
- Sato, T., Iwamoto, Y., Hashimoto, S., Ogawa, T., Furuta, T., Abe, S., Kai, T., Tsai, P.-E., Matsuda, N., Iwase, H., Shigyo, N., Sihver, L., Niita, K., 2018. Features of particle and heavy ion transport code system (PHITS) version 3.02. *J. Nucl. Sci. Technol.* 55, 684–690. <https://doi.org/10.1080/00223131.2017.1419890>.
- Sunderland, J.J., Erdahl, C.E., Bender, B.R., Sensoy, L., Watkins, G.L., 2012. Considerations, measurements and logistics associated with low-energy cyclotron decommissioning. Presented at the 14TH INTERNATIONAL WORKSHOP on TARGETRY and TARGET CHEMISTRY. Playa del Carmen, Mexico, pp. 16–20. <https://doi.org/10.1063/1.4773931>.
- The Swiss federal council, 2019. ORaP (Ordonnance sur la radioprotection).
- Toyoda, A., Yoshida, G., Matsumura, H., Masumoto, K., Nakabayashi, T., Yagishita, T., Sasaki, H., 2018. Evaluation of induced activity in various components of a PET-cyclotron. *J. Phys.: Conf. Ser.* 1046 <https://doi.org/10.1088/1742-6596/1046/1/012017>, 012017.
- Vincke, H., Theis, C., 2018. ActiWiz 3 – an overview of the latest developments and their application. *J. Phys.: Conf. Ser.* 1046 <https://doi.org/10.1088/1742-6596/1046/1/012007>, 012007.